Pol. J. Environ. Stud. Vol. XX, No. X (XXXX), 1-19
DOI: *10.15244/pjoes/224840* ONLINE PUBLICATION DATE: 2026-09-18

Original Research

Activated Carbon-Supported Palladium Nanoparticles: Synthesis Via Different Reducing Agents and Antibacterial Applications

Aisha M. Al Musharrafi[1], El-Said I. EL-Shafey[1]*, Nallusamy Sivakumar[2], Myo Tay Zar Myint[3], Mohamed Al-Kindi[4], Abdul Rahman Al-Nabhani[4], Saif Al-Mamari[5], Bushra Al-Daghari[5]

[1]Chemistry Department, College of Science, Sultan Qaboos University, PO Box 36, Postal Code 123, Muscat, Oman
[2]Biology Department, College of Science, Sultan Qaboos University, PO Box 36, Postal Code 123, Muscat, Oman
[3]Physics Department, College of Science, Sultan Qaboos University, PO Box 36, Postal Code 123, Muscat, Oman
[4]College of Medicine, Pathology Department, College of Medicine and Health Science, Sultan Qaboos University, P.O. Box 35, Muscat 123, Oman
[5]CAARU Center, College of Science, Sultan Qaboos University, PO Box 36, Postal Code 123, Muscat, Oman

Received: 22 February 2026
Accepted: 19 June 2026

Abstract

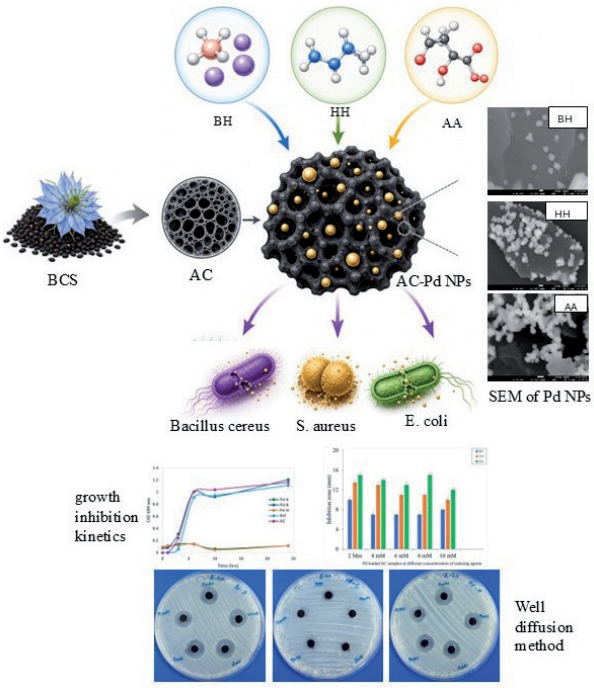

*e-mail: elshafey@squ.edu.om
Tel: +968 99822317
Fax: +96824141469
0000-0003-2406-4191

This study compares a green reducing agent (ascorbic acid, AA) with chemical reducing agents (borohydride, BH, and hydrazine hydrate, HH) for the immobilization of Pd^0 nanoparticles (NPs) onto activated carbon to evaluate their antibacterial properties. The activated carbon prepared from black cumin seeds was used as a substrate on which Pd nanoparticles (Pd NPs) were deposited in situ using the three reducing agents. The reducing agents were used over a concentration range of 2-10 mM at 20ºC. The Pd(0) loading was 45.4±0.5 (mg/g), 45.2±0.4 (mg/g), and 39.9±1.9 (mg/g) for BH, AA, and HH, respectively, when different amounts of reducing agents were used. X-ray powder diffraction (XRPD), scanning electron microscopy (SEM), and transmission electron microscopy (TEM) showed the presence of Pd NPs in different crystallite sizes, particle sizes, and morphologies. Pd particles produced by BH reduction were larger than those reduced by HH or AA. Crystallite size decreases as the concentration of the reducing agent increases for BH and AA, while with the increase in HH concentration, a slight increase in the average crystallite size was observed. The antibacterial efficacy against *S. aureus, B. cereus,* and *E. coli* was qualitatively assessed by inhibition zone size and quantitatively by turbidity. Growth inhibition zones for reduced Pd nanoparticles follow the order: AA>HH>BH. For the quantitative turbidity method, growth inhibition showed efficient antibacterial results for Pd NPs reduced by AA and HH more than those reduced by BH. This can be attributed to their smaller particle size compared with those reduced by BH.

Keywords: Pd nanoparticles, chemical reducing agents, ascorbic acid, antibacterial activity, activated carbon.

Introduction

Raising global health consciousness reflects the critical threat of infectious disease transmission and water quality issues. Consequently, it has become urgent to develop affordable and robust disinfectant systems that deactivate pathogenic microorganisms for water treatment and healthcare disinfection [1]. Antibiotics are potent medications for infectious diseases ranging from minor wounds to lethal diseases. However, due to the excessive use of antibiotics, drug-resistant bacteria are generated and become ubiquitous in the environment, posing a challenge to public health [2].

Antibiotic resistance has recently been considered among the top three public health threats by the World Health Organization (WHO) [2]. It is predicted that about ten million deaths will occur every year by 2050 because of infections caused by antibiotic-resistant bacteria worldwide [3]. Thus, metal nanoparticles have gained great attention as alternative antimicrobial agents because of their outstanding antibacterial properties [4]. Various metal nanoparticles, such as silver [5], gold [6], selenium [7], and copper [8], exhibit enhanced antimicrobial properties against antibiotic-resistant bacteria.

Among all nanoparticles, palladium nanoparticles (Pd NPs) have recently demonstrated considerable potential toward the development of antimicrobials and wound healing strategies, as well as exploration of antioxidant and anticancer therapeutics [9] due to their biocompatibility, adaptability to the environment, and physicochemical properties [10]. Several processes have been reported to produce Pd NPs, such as co-precipitation [11], sonochemical preparation [12], hydrothermal [13], electrochemical, and green/biological plant-extract methods [14]. Pd NPs exhibited antibacterial properties against *Staphylococcus aureus* [15, 16], *Bacillus subtilis*, *Escherichia coli*, *Klebsiella pneumoniae*, *Candida albicans*, and *Aspergillus niger* [16]. However, the variations in metal particle size, shape, and surface structure are critical aspects for enhancing their performance in biomedical applications [14, 17]. The size and morphology of palladium nanoparticles are affected by the synthesis factors, particularly the type and concentration of reducing agents [18, 19]. The selection of a reducing agent represents a critical decision in the synthesis of nanoparticles since it plays a multifaceted role, including influencing the reduction of metal precursors, nanoparticle size, morphology, stability, and antibacterial efficiency [20]. Palliyarayil et al. established the order Pd/C-$NaBH_4$ > Pd/C-HCHO > Pd/C-Ascorbic acid > Pd/C-Green tea for the activity of CO oxidation [21], while Yasmin et al. reported that CNT-Pd prepared with $NaBH_4$ exhibited superior performance for methanol oxidation compared to ascorbic acid and hydrazine [22]. These findings indicate that stronger reducing agents generate highly active catalysts. Additionally, strong reductants ($NaBH_4$, hydrazine) generally produce smaller and more uniform particle sizes due to rapid nucleation. Some studies of metal nanoparticles using different reducing agents in supported and unsupported systems are presented in Table 1. Pd NPs are considered efficient catalysts, allowing organic reactions to proceed faster and at lower temperatures, thereby improving atom economy and minimizing waste generation [21, 22].

In this study, activated carbon is used as a support for Pd NPs. The activated carbon was synthesized from black cumin seeds, which, to the best of our knowledge, has not been previously explored as a support medium

for Pd NPs in antibacterial applications. However, the novelty of this study extends beyond merely confirming the relationship between NP size and antibacterial performance. The primary contribution of this work lies in a systematic investigation of the influence of different reducing agents on the physicochemical characteristics of Pd NPs supported on biomass-derived activated carbon and the resulting impact on antibacterial activity.

Motivated by these considerations, this research focuses on the fabrication of antibacterial activated carbon-supported palladium nanoparticles with subsequent evaluation of their antibacterial performance. It is noteworthy that the scope of this research lies in the appropriate selection of the reducing agent that influences the efficacy of the antibacterial Pd NPs. Therefore, three reducing agents, including both sodium borohydride (BH) and hydrazine hydrate (HH), which are chemical reducing agents, and ascorbic acid (AA), which is a green reducing agent, were used to produce Pd NPs on activated carbon. Pd NP-loaded AC was physically and chemically characterized. The antibacterial properties were investigated against representative Gram-positive (*Bacillus cereus* and *S. aureus)* and Gram-negative (*E. coli*) strains.

Materials and Methods

Materials

All chemicals used were of analytical grade. $PdCl_2$ (99.7%) was used to prepare a solution of Pd(II) (2500 mg/L) in ultrapure water. Solutions of the reducing agents, including sodium borohydride ($NaBH_4$) (99.7%), hydrazine hydrate (N_2H_4) (80.0%), and ascorbic acid ($C_6H_8O_6$) (99.7%) in the range of 2–10 mM were prepared in ultrapure water. These chemicals, in addition to glutaraldehyde (99.5%), osmium tetroxide (99.7%), and ethanol (99.7%), were purchased from Sigma-Aldrich.

Preparation of AC-Pd NPs

Activated carbon (AC) was prepared from black cumin seeds via KOH activation (1:3) at 700ºC for one hour under a nitrogen atmosphere in a tube furnace (GSL-1700X, MTI Corporation, USA). The surface area of AC was estimated using an ASAP2020 instrument (Micromeritics, USA) via nitrogen adsorption at 77 K. Pd NPs were synthesized onto AC via both chemical reducing agents (BH and HH) and a green reducing agent (AA). In detail, 0.15 g of activated carbon was impregnated with 15 mL of Pd(II) solution (2500 mg/L, pH 1.39). The pH was adjusted by the suitable addition of HCl drops. The mixture was left to equilibrate at 20°C under continuous agitation (100 rpm) for 24 hours. Following the impregnation period, palladium-loaded AC was filtered, washed with deionized water, and dried at 105ºC. 5 mL aliquots of BH, HH, or ascorbic acid (AA) in the concentration range of 2-10 mM were mixed with the palladium-loaded AC, and the mixture was kept under agitation at 20ºC for 24 hours to promote *in situ* reduction of Pd(II) to Pd(0) on the AC surface. The produced AC-supported Pd NPs (AC-Pd NPs) were separated by filtration, repeatedly washed with deionized water to remove residual chemicals, and dried at 60°C to constant weight.

Determination of Pd Loading on AC

0.15 g of each of the AC-Pd NPs was treated with 5 mL of freshly prepared aqua regia (3 HCl:1 HNO_3). The digestion process was subjected to controlled heating at 70°C in a water bath for 1 hour to achieve quantitative dissolution of the palladium content. The resulting solution was filtered through Whatman

Table 1. Literature studies of different reducing agents for metal nanoparticles.

Metal Nanoparticles	Support Material	Reducing Agent(s)	Key Findings	References
Ag^0 NPs	Unsupported system	Chemical reduction	Demonstrated interaction between size and morphology effects on antibacterial activity.	[19]
Se^0 NPs	Unsupported system	Ascorbic acid, glutathione, cysteine	Reducing agents significantly affected nanoparticle stability, morphology, and antibacterial performance.	[20]
Pt^0, Pd^0, Rh^0, Ru^0	Unsupported system	$NaBH_4$, ascorbic acid, formic acid	Strong reducing agents produced smaller nanoparticles (<5 nm) with higher precipitation efficiency in solution.	[23]
ZnO NPs	Unsupported system	Chemical synthesis	Rod-shaped ZnO nanoparticles exhibited superior antibacterial activity.	[24]
Pd^0 nanocrystals	Unsupported system	Controlled crystal growth synthesis	Specific crystallographic facets enhanced membrane interaction and antibacterial performance.	[25]
Ag^0 NPs	Unsupported and AC-supported systems	$NaBH_4$, polyvinyl alcohol, glucose, and galactose	Particle size in solution (unsupported system) was 7-20 nm. In an AC-supported system, particles were larger (300-600 nm) due to agglomeration during the adsorption process.	[26]

filter paper (grade 42) to remove any residual insoluble materials. After several washings using ultrapure water, the clear filtrate and washings were collected and quantified using ICP-MS (Aurora M90, Bruker, USA).

Characterization of AC-Pd NPs

Material Characterization

X-ray powder diffraction (XRPD) was carried out using a Philips PW 1830 generator with a Philips PW 1050 powder goniometer (Philips, USA) using Cu-Kα radiation. Samples were inspected using field emission scanning electron microscopy (FESEM), JEOL/JSM 7600F (Jeol, Japan), at an accelerating voltage of 15 kV. Energy-dispersive spectroscopy (EDS) was also tested using a JEOL/JSM 7600F energy-dispersive analysis system (Jeol, Japan), which is attached to the JEOL / JSM 7600F scanning electron microscope. Fourier transform infrared (FTIR) spectra were performed in transmission mode using an FTIR spectrometer (Spectrum BX, PerkinElmer, USA) through a wavelength range of 4000-400 cm^{-1} with background subtraction. The AC surface was examined using X-ray photoelectron spectroscopy (XPS, Scienta Omicron, Germany) with Al-Kα (hv = 1486.6 eV) at 15 kV as the incident X-ray. The XPS data were analyzed using Casa XPS software (Casa Software Ltd, UK) with a Shirley-type background. The binding energies analyzed were calibrated using the C1s peak at 284.6 eV. The high-resolution transmission electron microscopy (HRTEM) measurement was carried out using JEOL JEM-2100F (Japan) at an accelerating voltage of 200 kV.

Antibacterial Tests

The antibacterial efficiency of the synthesized AC-Pd NPs was evaluated against isolated bacterial strains (clinical isolates, obtained from the Microbiology Department, College of Medicine, Sultan Qaboos University). Antibacterial effectiveness was evaluated using the well diffusion method, and growth inhibition kinetics for 24 hours of incubation against *E. coli*, *B. cereus,* and *S. aureus*. For the well diffusion method, the bacteria were sub-cultured in sterile nutrient broth at 37°C in an incubator for 24 hours. The test was performed by inoculating 100 µL of each strain onto nutrient agar plates and spreading with a sterile glass rod swab. Wells of 6 mm diameter were punched in the nutrient agar under a fume hood and near a flame. 6 mg of AC-Pd NP samples and 100 µL of deionized water were poured into the wells. After 24 hours of incubation at 37ºC, the expansion of the growth inhibition zone was measured in millimeters (mm) using a digital caliper. The experiment was repeated 3 times. Activated carbon was used as a negative control [27]. For the positive control, 100 µL of 0.01 M ciprofloxacin and clarithromycin in aqueous solution was injected into the agar well (6 mm diameter). After 24 hours of incubation at 37ºC, the expansion of the inhibition zone was measured in millimeters (mm).

For the growth inhibition kinetics, an amount of 90 mg of AC-Pd NPs was combined with sterilized nutrient broth, followed by the addition of 100 µL of bacterial culture. The samples were incubated in a shaker incubator at 37ºC at 130 rpm for 24 hours. Growth was evaluated by measuring optical density spectrophotometrically at 600 nm at predetermined intervals.

FE-SEM of Bacteria Control and the Inhibition Zone

Field-emission scanning electron microscopy (FE-SEM) imaging was carried out to evaluate the antibacterial properties of AC-Pd NPs. Both untreated bacteria (control) and bacteria from the inhibition zone were fixed with 2% glutaraldehyde at room temperature overnight to preserve cellular ultrastructure, followed by post-fixation using 1% osmium tetroxide for 1 hour at room temperature. Samples were dehydrated through a graded ethanol series ranging from 25% to 100% and dried at room temperature after using hexamethyldisilane dehydrant. The dried cells, after mounting on a stub and coating with platinum, were examined under FESEM [28, 29].

Results and Discussion

Metal Nanoparticles' Antibacterial Properties

Infections caused by waterborne bacteria are considered one of the major causes of human mortality, with about 1.2 billion people without access to clean water [30]. Metal nanoparticles have emerged as a promising technology for antibacterial applications in water treatment, having a direct impact on public health. Traditional treatment of bacteria can lead to antibacterial resistance, which is predicted to become one of the most serious challenges to human and animal health soon [31]. Due to their extremely small size and high surface-area-to-volume ratio, nanoparticles show enhanced chemical reactivity and antimicrobial efficiency compared to conventional disinfectants. Nanoparticle-based disinfection offers several advantages over chlorination, ozonation, and UV disinfection. Chlorination has long been the most common method for water disinfection because it is inexpensive and effective against many pathogens. However, chlorine reacts with natural organic matter in water, forming harmful disinfection by-products such as trihalomethanes and haloacetic acids, which are associated with adverse reproductive effects and cancer risks [32]. In addition, some bacteria show resistance to chlorination, such as Cryptosporidium [33]. UV irradiation as a water disinfectant generates hydroxyl radicals in water, which inhibit bacterial

growth due to DNA destruction and protein denaturation of the microorganisms [34]. However, some bacteria, such as *Deinococcus radiodurans*, can still survive high doses of ionizing UV radiation [35]. Ozonation is another disinfectant that can destroy pathogens via oxidation. In addition to being expensive, it generates toxic bromate by-products in water. It can also produce harmful byproducts in water, including peracetic acid, hydrogen peroxide, and iodine [34].

Metal nanoparticles have attracted major interest as an alternative or complement to conventional antibiotics. This is due to their broad spectrum of antimicrobial activity, as they can act against a wide range of microorganisms, such as Gram-positive bacteria, Gram-negative bacteria, fungi, and some viruses [36]. For example, Ag NPs can damage membranes, proteins, and DNA of bacteria simultaneously; however, antibiotics such as penicillin mainly target cell-wall synthesis [37]. In addition, bacteria can adapt to antibiotics, showing resistance, while metal nanoparticles use multiple mechanisms, making the development of resistance more difficult [38]. In fact, metal nanoparticles are effective against multidrug-resistant bacteria. Currently, copper and silver nanoparticles are particularly effective against resistant pathogens in hospitals [39]. Bacteria develop biofilms for protection against antibiotics; however, metal nanoparticles can penetrate the biofilms and kill the microbes. Finally, metal nanoparticles are stable under harsh conditions of heat, pH changes, and enzymatic activities [36].

Reduction of Pd(II) to Pd^0 Nanoparticles

Activated carbon was prepared from black cumin seeds using KOH activation at 700°C for one hour under a nitrogen atmosphere. The BET surface area of AC was 1175 m^2/g. Most of the surface area was microporous (1080.1 m^2/g), accounting for 92% of the total BET surface area of AC. The mesoporous surface area was 94.9 m^2/g, and the average pore diameter was 21.82 A°. Pd(II) was loaded onto the carbon, followed by immersion in the different reducing agents. AC-Pd NPs were examined using XRPD, SEM, TEM, EDS, XPS, and FTIR.

The three reducing agents (BH, HH, and AA) were reported to be effective reductants for the reduction of Pd(II) to Pd [22]. Varying the concentration of reducing agents showed no significant variation in the amount of Pd on AC (Fig. 1). The amount of 39.9±1.9 mg/g of Pd-loading on AC using HH seems slightly less than that reduced using BH of 45.4±0.5 mg/g or AA (45.2±0.4 mg/g). However, since the reducing agents provide the electrons needed for the reduction reaction of Pd(II) to Pd^0, variation in the concentration of the reducing agents may directly influence the reaction kinetics and, subsequently, the nucleation and growth rate of nanoparticle formation [40, 41]. Since the pH of the sorption solution is acidic (pH 1.39), the standard reduction potentials of BH, HH, and AA, in addition to that of Pd(II) vs. HSE, and the half-cell reactions are presented in Eqs. (1)-(4).

$$BH_4^- + 3H_2O = B(OH)_3 + 7\,H^+ + 8\,e^-$$
$$E^o = -0.48\ V\ [40, 42] \quad (1)$$

$$N_2H_5^+ = N_2 + 5H^+ + 4\,e^-$$
$$E^o = 0.230\ V\ [40] \quad (2)$$

$$C_6H_8O_6 = C_6H_6O_6 + 2H^+ + 2\,e^-$$
$$E^o = 0.077\ V\ [40] \quad (3)$$

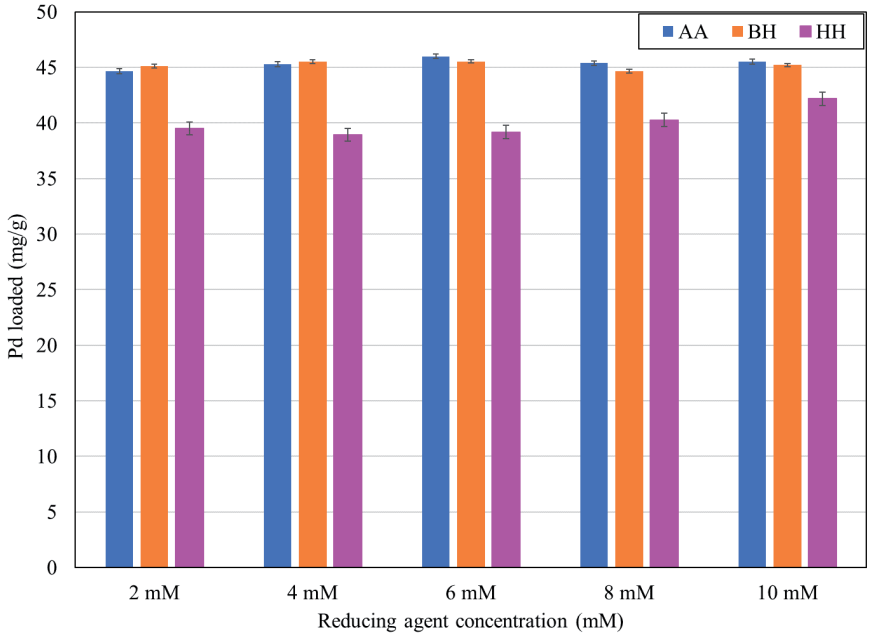

Fig. 1. Pd loading on AC using different reducing agents between 2 and 10 mM at 20°C.

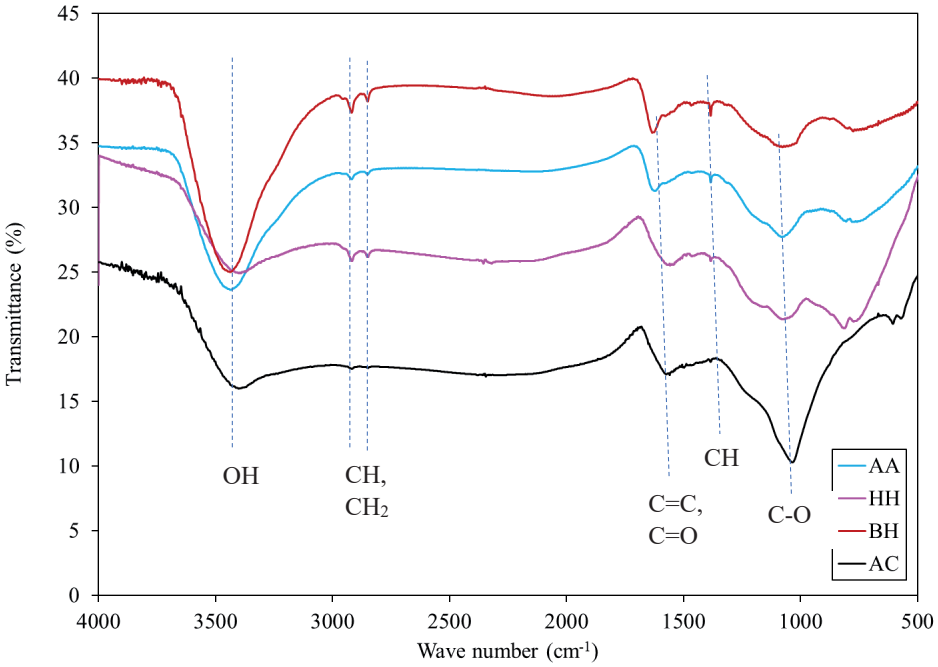

Fig. 2. FTIR of AC and Pd-loaded AC using different reducing agents at 2 mM concentration.

$$Pd^{2+} + 2\ e^- = Pd^0$$
$$E^o = 0.951\ V\ [43] \qquad (4)$$

FTIR

FTIR spectra of AC and AC-Pd NPs are presented in Fig. 2. The band at ~3437 cm^{-1} corresponds to the stretching vibration of -OH. The band between 1628-1560 cm^{-1} corresponds to C=C or C=O stretching vibration. However, the bands between 1300 cm^{-1} and 1000 cm^{-1} are related to C-O stretching vibrations in aldehydes, anhydrides, ethers, and other C-O groups [44]. The shoulders assigned at 2919 cm^{-1} and 2850 cm^{-1} are related to C-H stretching vibrations in CH and CH_2 groups [44]. Such shoulders did not appear for AC before Pd-loading via reduction. In addition, the band at 1385 cm^{-1}, which is related to C-H bending vibration, did not appear for AC. It is obvious that the intensity of the -OH group has increased after reduction, particularly for BH and AA. This is mostly related to the reduction of aldehydes and ketones on the AC surface to alcohols by the reducing agents [45]. There is also a decrease in the intensities of bands in the range of 1300-1000 cm^{-1} (C-O) after reduction, indicating that the reducing agents also reduce some carbon–oxygen functionality on the AC surface [45-47].

XRPD, SEM and TEM

XRPD analysis confirms the presence of crystalline Pd NPs (Fig. 3). Characteristic diffraction peaks were detected in all samples at 2θ of 40.34°, 46.71°, 68.21°, 82.13°, and 86.71°, with *h*, *k*, and *l* indices of (111), (200), (220), (311), and (222) of a face-centered cubic (fcc) palladium structure [48]. However, as the reducing agent changes, the most intense peak at a 2θ value of ~ 40° corresponding to the (111) plane shows significant changes, indicating variation in the degree of anisotropy of Pd. Higher intensity was observed for Pd NPs reduced by BH and AA compared to those reduced by HH (particularly at 10 mM concentration of HH). The crystallite size of Pd in Pd NPs (D) was calculated using the Scherrer equation, Eq. (5) [49].

$$D = K\lambda/(b\cos\theta) \qquad (5)$$

$$\beta = (\pi/180)\ FWHM \qquad (6)$$

K refers to the Scherrer constant, λ is the wavelength of the X-ray beam applied, β is the full width at half maximum (FWHM) of the peak in radians (Eq. (6)), and θ is the Bragg angle. A *K*-value of 0.90 works well with spherical crystals [49].

The average crystallite size was calculated using the first 5 diffraction peaks between 2q of 40.09 and 86.58°. The average crystallite size of Pd is presented in Fig. 4 using different concentrations of reducing agent at 20°C for initial Pd(II) concentrations of 2500 mg/L. It seems that the average crystallite size decreases as the concentration of reducing agent increases for both BH and AA. The higher concentrations of BH and AA lead to a rapid reduction of Pd(II) ions, forming a smaller crystallite size of Pd. However, with the increase in HH concentration, a slight increase in the average crystallite size was observed (Fig. 4). As shown in Fig. 4, the maximum crystallite size of Pd appears for 2 mM concentration of BH and AA, and 10 mM of HH.

In a similar study, the crystal size of Ag^0 NPs was found to decrease with increasing concentration of reducing agent (trisodium citrate) [50].

The morphology of the synthesized Pd NPs was significantly influenced by the reducing agent used, as confirmed by the SEM images presented in Fig. 5. Reduction with BH produced anisotropic structures, including multifaceted crystals and irregularly shaped nanoparticles. Notably, using HH yielded Pd NPs with an octahedral structure. In contrast, numerous spherical nanoparticles of palladium were predominantly formed when ascorbic acid was used. The average particle size

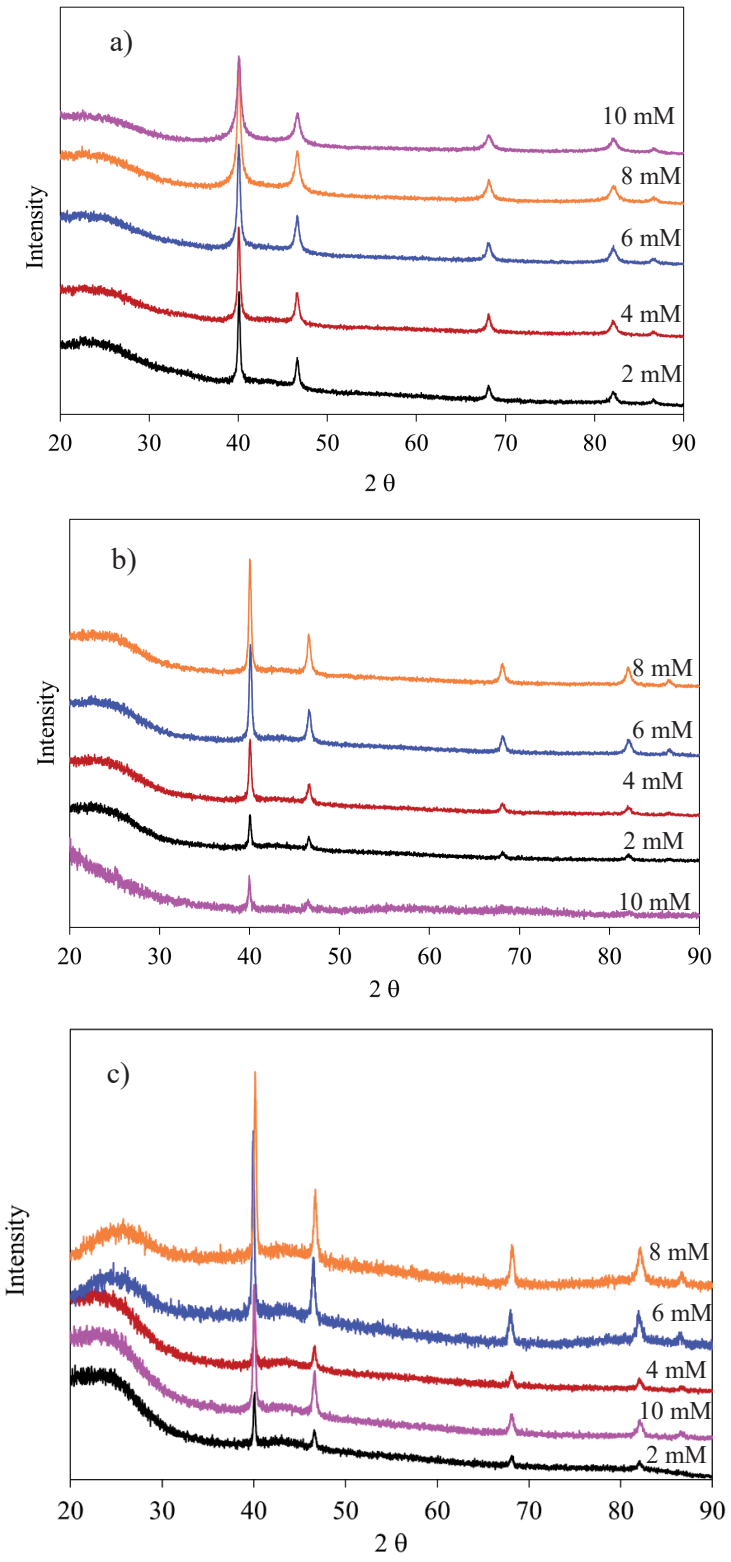

Fig. 3. XRPD of Pd NPs on AC using a) BH, b) HH, and c) AA at different concentrations between 2 and 10 mM.

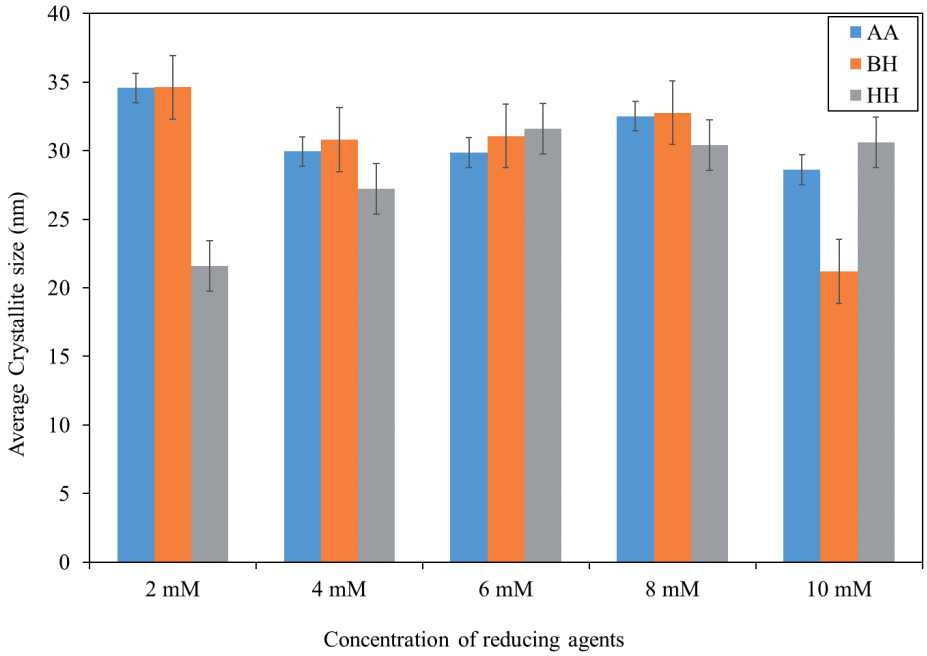

Fig. 4. Average crystallite size of Pd^0 using the Scherrer equation at different concentrations of the reducing agents.

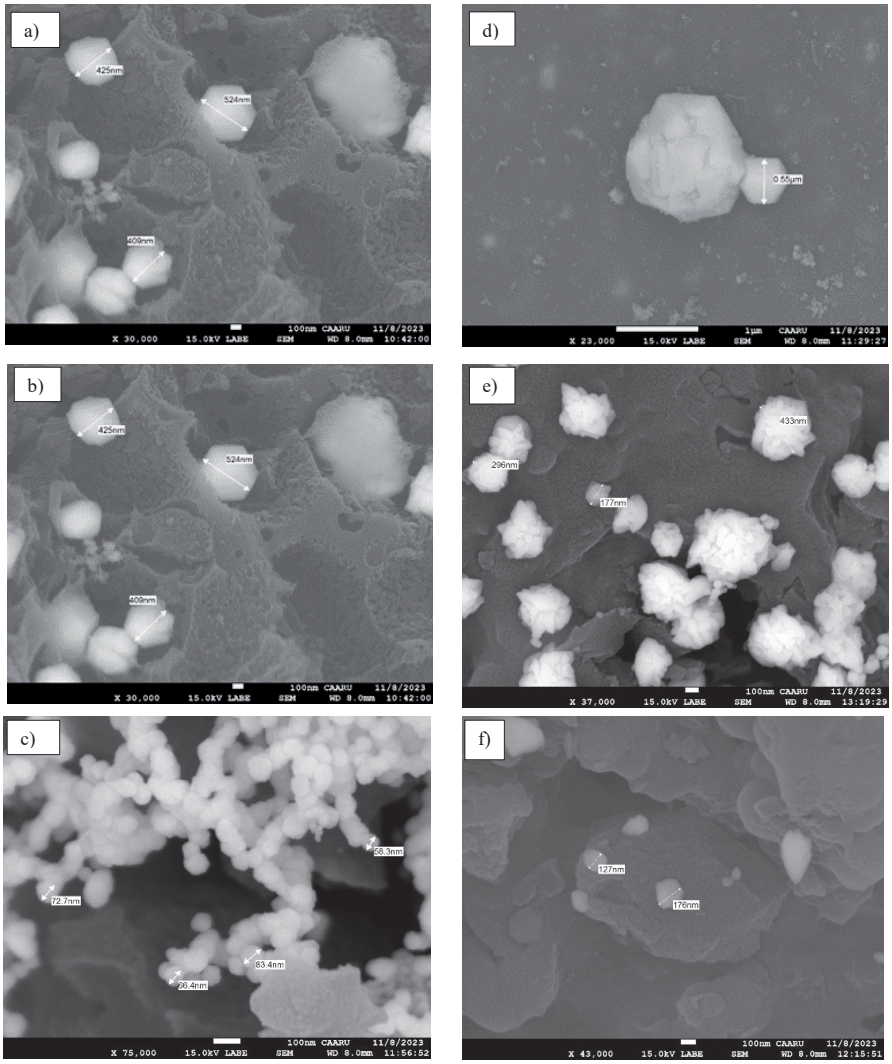

Fig. 5. SEM images of Pd particles reduced by BH: a) 2 mM and d) 10 mM; HH: b) 2 mM and e) 10 mM, and AA: c) 2 mM and f) 10 mM.

of Pd was estimated using ImageJ software from SEM images. The average particle size of Pd^0 was 61±8 nm, 87±20 nm, and 471±60 nm when 2 mM of AA, HH, and BH were used, respectively (Fig. 5). The average size of Pd NPs is less than 100 nm for AA and HH, while for BH, it is larger than 100 nm. Pd NPs appear more homogeneous in size for AA than for HH. However, when the larger concentrations of 10 mM of the reducing agents were used, the average Pd particle size appears larger than 100 nm, with values of 138±80 nm, 272±80 nm, and 1159±500 nm for 10 mM AA, HH, and BH, respectively (Fig. 5). BH shows an exceptionally large particle size.

With the increase in the concentration of the reducing agent, an increase in the size of particles, with a decrease in the number of particles, is obvious (Fig. 5) [51].

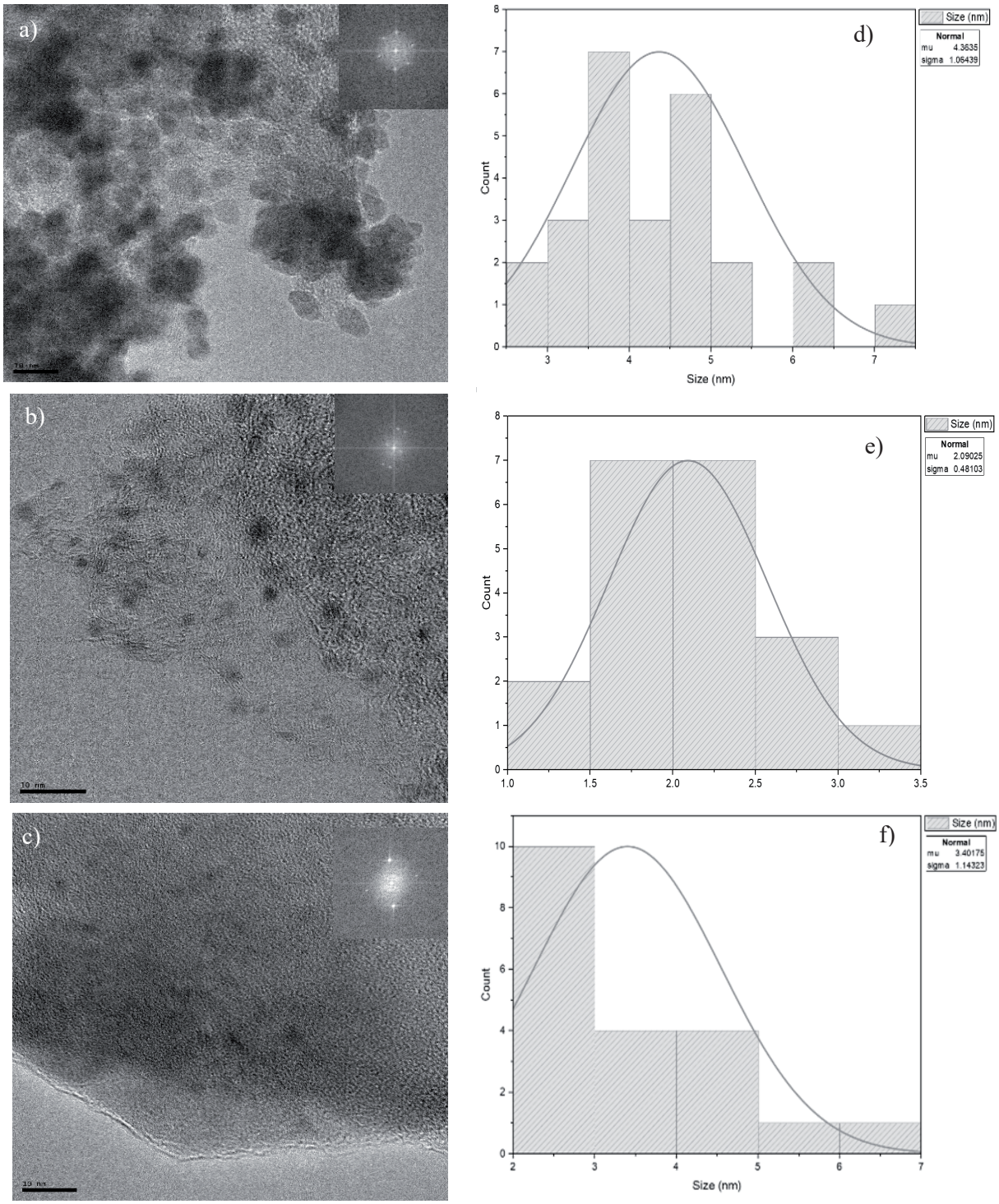

Fig. 6. TEM images of Pd NPs reduced using 6 mM of a) BH, b) HH, and c) AA, and the corresponding particle size distributions for Pd NPs reduced using 6 mM of d) BH, e) HH, and f) AA.

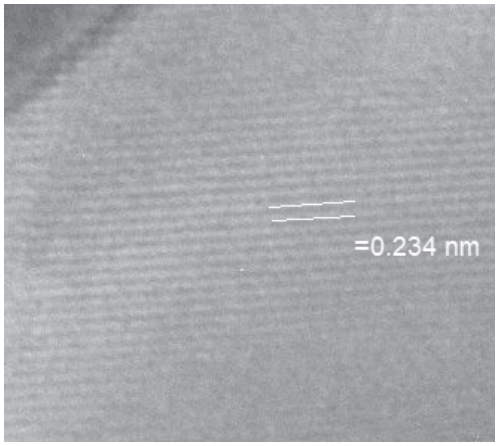

Fig. 7. HRTEM image of Pd^0 particles on AC.

This is indicative of a coalescent growth mechanism where smaller particles come together to form larger particles, reducing the total number of particles [51]. This is clearly demonstrated in the SEM images for Pd NPs produced using 10 mM BH (Figs. 5a) and d)). TEM images and particle size distribution histogram of Pd NPs produced using 6 mM of the reducing agents are presented in Fig. 6(a-f). A lattice spacing of 0.234 nm was identified in TEM images, indicating the presence of Pd crystals with 111 *h k l* indices (Fig. 7). According to TEM images, all synthesized Pd NPs are well dispersed in spherical and non-spherical morphologies. The average particle size of Pd NPs from TEM is 2.7-7 nm, 1.4-3 nm, and 2–7 nm for samples reduced by BH, HH, and AA, respectively (Fig. 6(d-f)).

As presented in Figs. 5 and 6, there is a large difference in the Pd NP size estimated from SEM and TEM images, as both are different techniques with different sample preparation methods. TEM provides better resolution (0.1 nm) and uses the transmission mode technique [52, 53]. SEM has 1 nm resolution and uses the secondary electron detection method for imaging [54]. Thus, the particles on the AC surface measured by SEM are larger in size than those measured by TEM. Moreover, the diffraction pattern in the back focal plane appears as concentric rings, indicating polycrystalline phases of Pd (Fig. 6(d-f)) [55]. The TEM image revealed that the Pd^0 NP size within the porous structure is probably controlled by the pore size within which they were deposited, as the porous structure of AC is rigid and non-flexible [54, 56]. On the other hand, Pd particles deposited on the AC surface have no such limitation in particle growth, with more ability for Pd atoms to aggregate, forming larger Pd particles. The size estimated from XRPD by the Scherrer equation exhibited an average crystallite size within the Pd particles [55], where several crystallites are available in a Pd particle. In general, metal nanoparticles formed by reduction in solution become smaller in size when a larger concentration of reducing agent is used. For example, the size of Au^0 nanoparticles in solutions decreased on raising the concentration of caffeic acid (reducing agent) [57]. Another study showed that small-sized Ag^0 nanoparticles in solution require an excess of strong reducing agent, which facilitates instant nuclei generation, resulting in the formation of uniformly sized silver colloids [58]. In a previous study [26], colloidal Ag^0 NPs with a particle size of 7-20 nm were generated using different reducing agents of $NaBH_4$, polyvinyl alcohol, glucose, and galactose in solution. However, in the same study [26], using these reducing agents for Ag(I) reduction has led to a larger particle size (300-600 nm) on AC. The increased sizes of Ag^0 NPs on AC are related to particle agglomeration during the adsorption process [26]. In the present study, in which activated carbon was used as a support, larger concentrations of reducing agents formed larger Pd particles on AC due to particle agglomeration [26], but with a smaller average crystallite size. In another study [59], Ag^0 nanoparticles were prepared using Coccinia grandis peel extract onto AC. The particle size of Ag^0 was (15-20 nm) from TEM, 50.2 nm from SEM, and the average crystallite size measured from X-ray diffraction was (15-18 nm) [59]. The particle size measured by SEM was also found to be larger than that measured by TEM, and this was attributed to particle agglomeration onto the AC surface [26]. Another study confirmed the significant variation in the estimated particle size of nanocrystalline mackinawite with the methods used [60].

EDS Analysis

The EDS spectra and elemental analysis of Pd NP_s on AC presented in Table 2 show higher palladium content when a 10 mM concentration of reducing agents was used than when a 2 mM concentration was used. BH shows a higher Pd % than the other reducing agents, and this could be related to the larger particle sizes of Pd developed by using BH, where a higher amount of Pd is present on the surface of AC.

XPS Analysis

XPS spectra of Pd3d for Pd-loaded AC at initial concentrations of 2500 mg/L were investigated using 2 mM and 10 mM reducing agents. The XPS technique reveals the surface structure to a depth of 10 nm [44]. The deconvolution of palladium peaks for each reducing agent at 2 mM and 10 mM concentrations is presented in Fig. 8(a-f). The peaks in the range of 335.6-336.7 and 340.8-342.1 eV refer to Pd for $Pd3d_{5/2}$ and $Pd3d_{3/2}$, respectively. However, the peaks at 337.2-337.8 eV and 342.5-343.0 eV refer to Pd(II) for $Pd3d_{5/2}$ and $Pd3d_{3/2}$, respectively [27, 61]. As presented in Table 3, for $3d_{5/2}$ peaks (335.6-336.7 eV, and 337.2-337.8 eV), the percentages of Pd(0) and Pd(II), on Pd-loaded AC (for 2 mM concentration) were 75.9 and 24.1%, respectively, for BH, 42.2 and 67.8%, respectively, for

Table 2. EDS analysis of Pd-loaded AC.

Concentration mM	Reducing agent	Element (%)					
		Pd^0	C	O	Al	Cl	Cu
2	BH	70.7	22.4	4.7	2.2	-	-
	HH	45.8	34.0	3.7	5.3	7.9	3.2
	AA	57.0	34.9	6.2	1.3	-	-
10	BH	85.5	10.9	1.5	2.1	-	-
	HH	72.2	21.8	3.6	1.4	0.9	-
	AA	83.9	12.4	2.9	0.8	-	-

Table 3. Pd loading on AC and percentages of Pd(0) and Pd(II) at Pd $3d_{5/2}$ and Pd $3d_{3/2}$ determined by XPS.

Reducing agent		Amount of Pd^0 reduced (mg/g)	$3d_{5/2}$		$3d_{3/2}$		Pd state
Type	Concentration mM		Binding energy (eV)	Pd (%)	Binding energy (eV)	Pd (%)	
BH	2	45.11	336.6	75.9	341.9	61.3	Pd^0
			337.5	24.1	342.6	38.7	Pd^{2+}
	10	45.21	336.7	75.9	342.0	61.3	Pd^0
			337.6	24.1	342.7	38.7	Pd^{2+}
HH	2	39.52	335.6	42.2	340.8	32.4	Pd^0
			337.8	57.8	343.0	67.6	Pd^{2+}
	10	42.18	335.6	65.5	340.9	61.8	Pd^0
			337.5	34.5	342.5	38.2	Pd^{2+}
AA	2	44.67	336.7	51.8	342.1	38.1	Pd^0
			337.2	48.2	342.6	61.9	Pd^{2+}
	10	45.29	335.6	43.6	340.8	35.0	Pd^0
			337.7	56.4	342.9	65.0	Pd^{2+}

HH, and 51.8 and 48.2%, respectively for AA. With the increase in the concentration of the reducing agents to 10 mM, for $3d_{5/2}$ peaks (335.6-336.7 eV, and 337.5-337.7 eV), the percentages of Pd(0) and Pd(II), on Pd-loaded AC were 75.9 and 24.1%, respectively for BH, 65.5 and 35.5%, respectively for HH, and 43.6 and 56.4%, respectively, for AA.

On the other hand, for $3d_{3/2}$ peaks (340.8-342.1 eV, and 342.5-343.0 eV), the percentages of Pd(0) and Pd(II), on Pd-loaded AC (for 2 mM concentration) were 61.3 and 38.7%, respectively, for BH, 32.4 and 67.6%, respectively, for HH, and 38.1 and 61.9%, respectively, for AA. However, using 10 mM of the reducing agents, for $3d_{3/2}$ peaks (340.8-340.9 eV, and 342.5-342.9 eV), the percentages of Pd(0) and Pd(II) on Pd-loaded AC were 61.3 and 38.7%, respectively, for BH, 61.8 and 38.2%, respectively, for HH, and 35.0 and 65.0%, respectively, for AA. It appears from these values that Pd(0) from XPS using the peak of $3d_{5/2}$ follows the order of BH>AA>HH when 2 mM of the reducing agent was used, while for a 10 mM concentration of the reducing agent, it follows the order of BH>HH>AA.

Antibacterial Activity

Pd-loaded AC shows an antibacterial effect presented by the growth inhibition zone size. Fig. 9 shows the inhibition zones for *S. aureus* (Fig. 9(a-c)), *B. cereus* (Fig. 9(d-f)), and *E. coli* (Fig. 9(g-i)), for Pd-loaded AC using 2-l0 mM of BH, HH, and AA, respectively. Fig. 10 shows the variation of the inhibition zones of the three bacteria at the different concentrations of the reducing agents. The inhibition zone for bacterial growth by Pd NPs follows the order of AA>HH>BH for most of the concentrations of the reducing agents. The inhibition zone also decreases as the reducing agent concentration increases for AA and HH, whereas for BH, the inhibition zones appear the smallest, with no clear trend.

As presented in Table 4, there is a clear correlation between Pd particle size (nm) and the inhibition zone

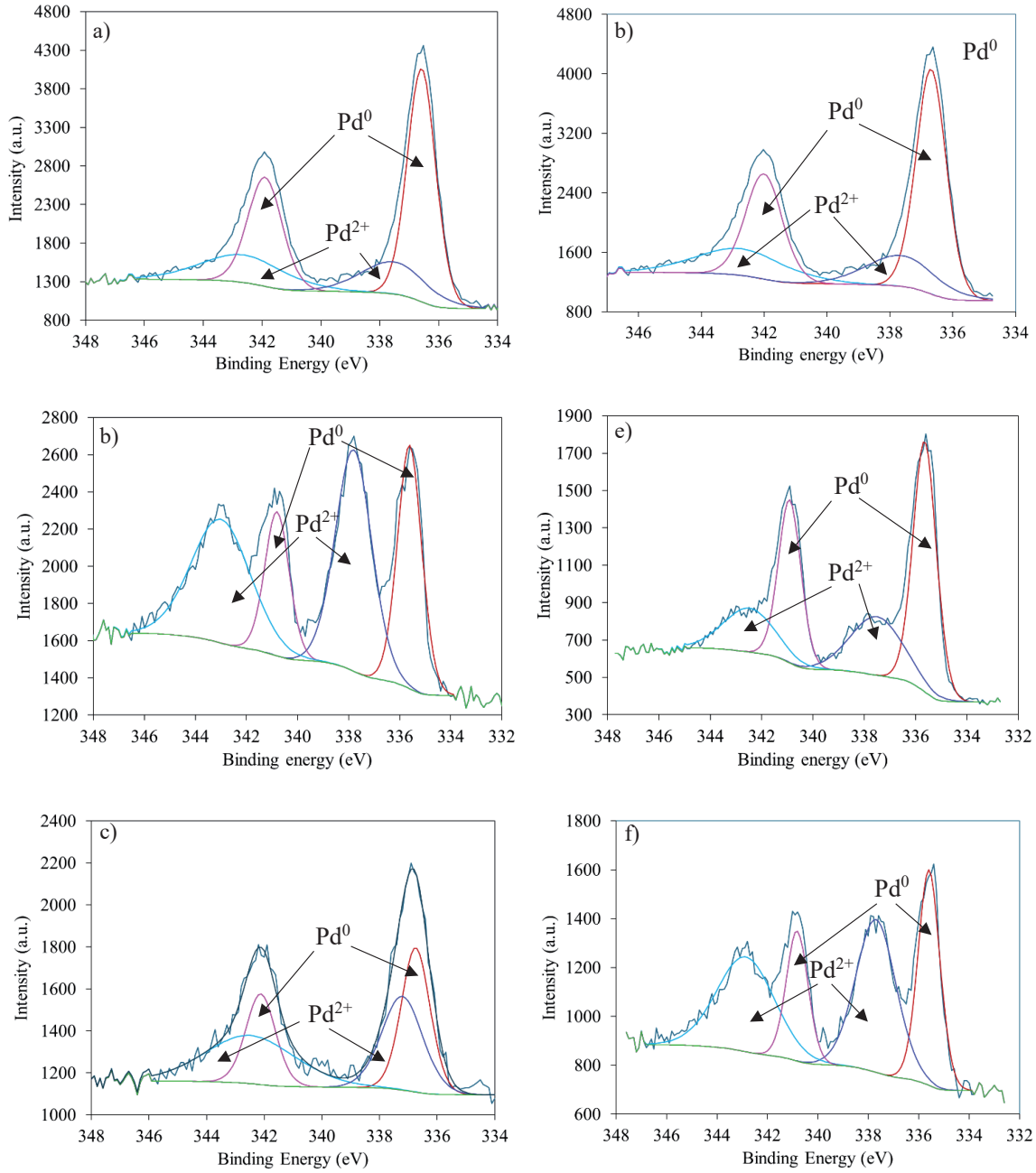

Fig. 8. Deconvolution of Pd3d for Pd reduced by a) 2 mM BH, b) 10 mM BH, c) 2 mM HH, d) 10 mM HH, e) 2 mM AA, and f) 10 mM AA.

(mm) for the three bacteria under investigation. As the concentration of the reducing agent increases, the particle size (by SEM) increases, and the inhibition zone decreases. Similar results were found when Pd particles were used against *S. aureus* and *B. subtilis* [62]. Other studies showed that Pd proved efficient against bacteria such as *E. coli*, *S. aureus*, and *C. sakazakii* [63-65]. The inhibition zone data for different bacteria with varying Pd^0 particle sizes were analyzed using one-way ANOVA. The results showed that the F value was 0.383, which was less than F_{crit} (3.68), and the p value (0.69), which is greater than 0.5. These values indicate that the variation in the inhibition zones of the different bacteria across the different particle sizes of Pd NPs is similar, with no significant differences among them. Statistical analysis is presented in Table S1 (Supplementary Material).

For the positive control, the inhibition zones for ciprofloxacin (Fig. 11(a-c)) were 35.8±0.6 mm for *B. cereus*, 26.5±0.4 mm for *S. aureus*, and 12.7±0.6 mm for *E. coli.* However, when clarithromycin was used, the inhibition zones (Fig. 11(d-f)) were 27±1 mm for *B. cereus*, 25±0.7 mm for *S. aureus,* and 38±1 mm for *E. coli.* Using the antibiotics (100 mL, 0.01 M of each) shows larger growth inhibition zones compared with those of Pd NPs (Fig. 10(a-c)). The antibiotics

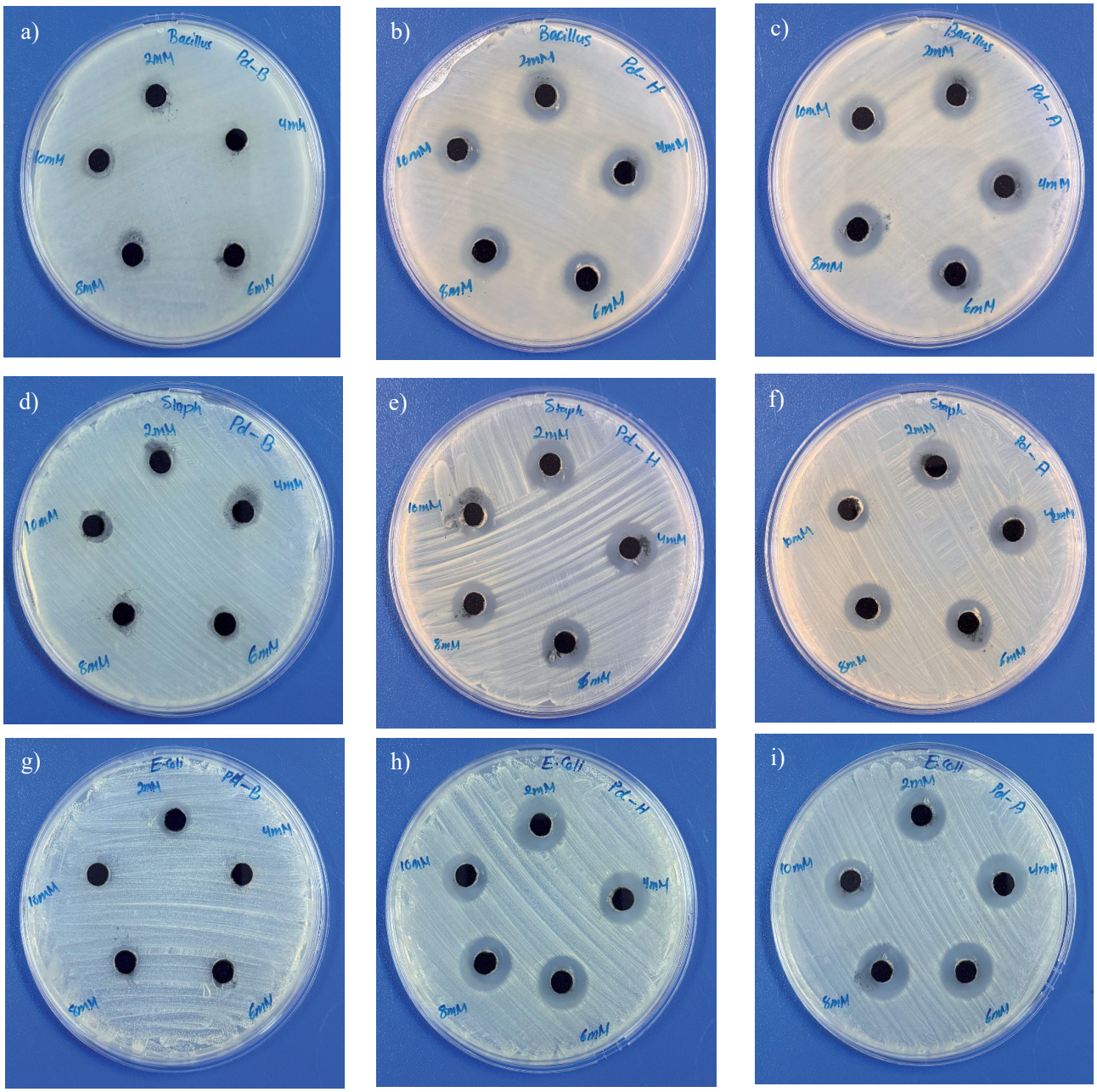

Fig. 9. Images of inhibition zones of Pd NPs for (a-c) *B. cereus*, (d-f) *S. aureus*, and (g-i) *E. coli* using BH (a, d, g), HH (b, e, h), and AA (c, f, i), respectively, for concentrations of reducing agents between 2 mM and 10 mM.

Table 4. Pd^0 particle size (by SEM) vs the inhibition zone using 2 mM and 10 mM of the reducing agent.

Reducing agent	Concentration mM	Pd^0 particle size by SEM (nm)	Bacterial inhibition zone (mm)		
			S. aureus	*B. cereus*	*E. coli*
AA	2	60.9±8.5	15.2±0.3	15.8±0.3	14.5±0.5
	10	137.5±82.9	13.3±0.3	14.2±0.3	12.3±0.6
HH	2	86.7±18.6	14.2±0.3	14.2±0.3	13.3±0.3
	10	272.2±82.9	10.7±0.3	11.8±0.3	10.0±0.5
BH	2	471.0±58.8	9.2±0.3	10.0±0.5	10.0±0.5
	10	1158.7±527.3	8.8±0.3	9.5±0.5	7.5±0.5

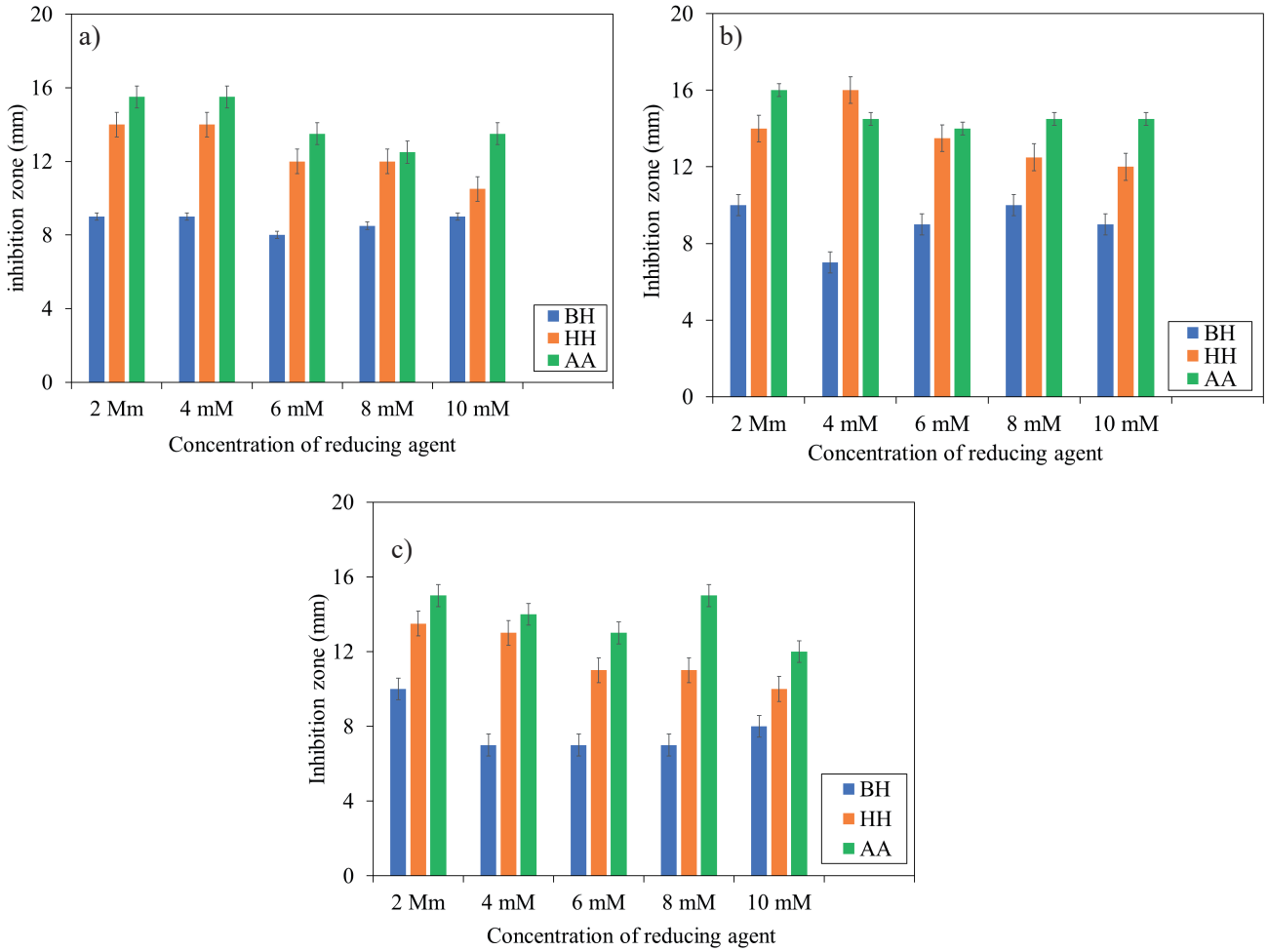

Fig. 10. Inhibition zone (mm) at different concentrations of reducing agent for a) *S. aureus,* b) *B. cereus*, and c) *E. coli,* respectively.

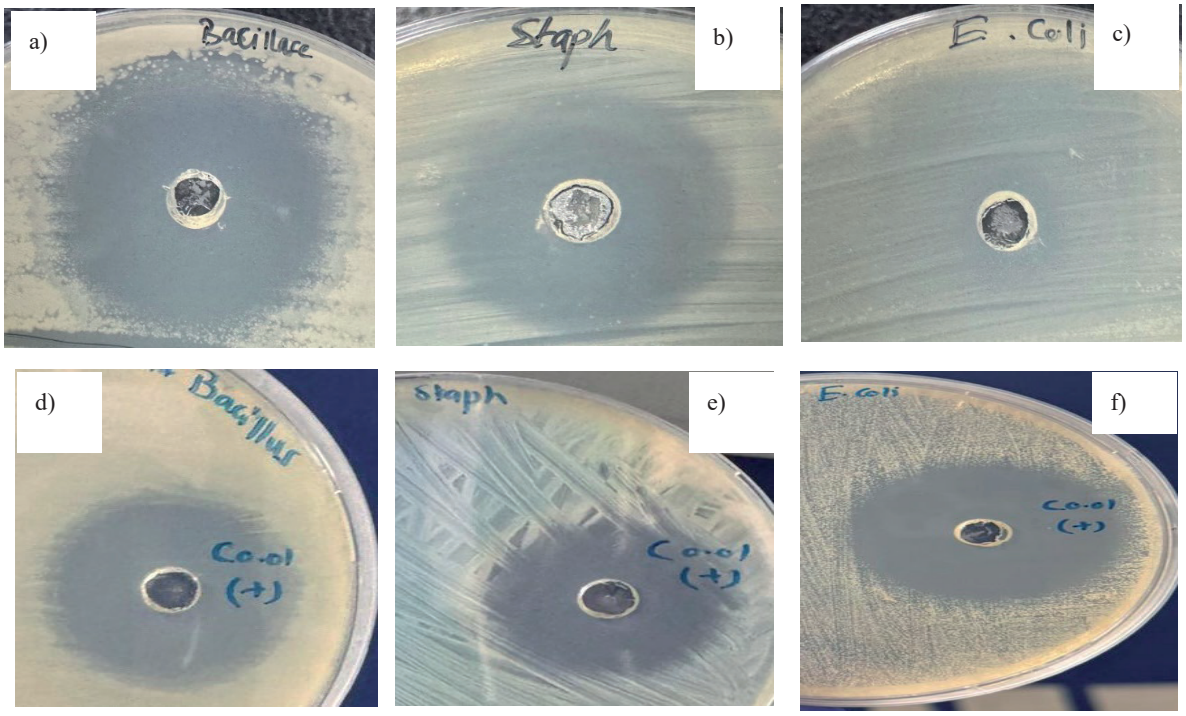

Fig. 11. Images of inhibition zones of ciprofloxacin for a) *B. cereus*, b) *S. aureus,* and c) *E. coli*, and of clarithromycin for d) *B. cereus*, e) *S. aureus,* and f) *E. coli* using 100 ml of 0.10 M of each.

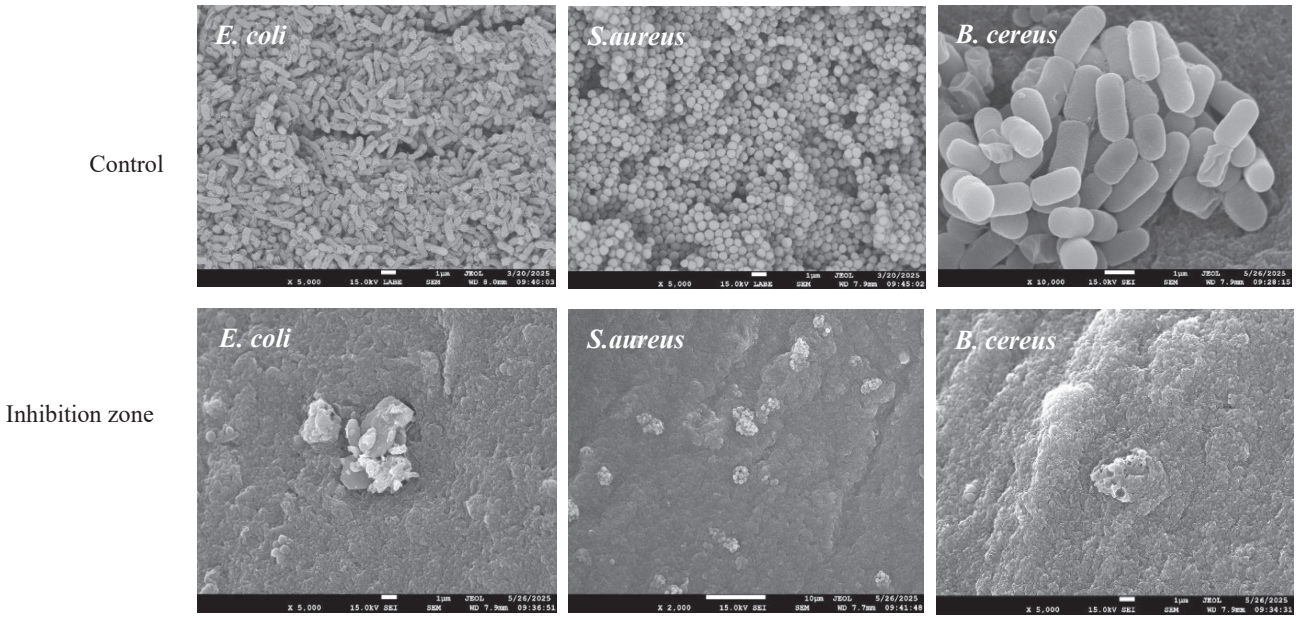

Fig. 12. SEM images of the control and the growth inhibition zones of the bacteria.

were introduced as an aqueous solution, which has better diffusion in the agar than solid Pd NPs on AC. In addition, the amount of the antibiotic introduced into the agar well was larger (331.4 mg of Ciprofloxacin, 747.95 mg of clarithromycin) than the amount of Pd NPs introduced into the agar well with 6 mg of loaded AC (272 mg for BH, 271 mg for AA, and 238 mg for HH). The bacteria were examined by SEM for the control and the growth inhibition zone (Fig. 12). It is obvious that the bacteria were not able to grow in the inhibition zone around the Pd-loaded particles.

For the quantitative (turbidity) antibacterial study, Pd-loaded AC reduced by 2 mM of the reducing agent was tested against *E. coli* (Fig. 13a)), *S. aureus* (Fig. 13b)), *and B. cereus* (Fig. 13c)) at 37ºC over 24 hours. The growth curve pattern of the bacteria acts as an empirical model of the evolution of a quantity over time. Compared with the control sample, Pd-loaded AC samples exhibit antibacterial activity. AC alone appeared to act as a nutrient source for the bacteria (Fig. 13(a-c)). Growth inhibition reached 7.9, 89.4, and 89.4% for *E. coli*, 5.89, 90.9, and 84.9% for *S. aureus,* and 12.4, 90.1, and 90.7% for *B. cereus* for Pd NPs reduced on AC by 2 mM of each of BH, AA, and HH, respectively. Pd NPs reduced by AA and HH show more effective antibacterial properties than Pd NPs reduced by BH, and this is related to the larger Pd particles reduced by BH. The antibacterial mechanism of Pd NPs observed in this study can be attributed to several mechanisms. The most important mechanism is the ability of NPs to generate reactive oxygen species (ROS) and their affinity to associate closely with R-SH groups. The metal ions in the NPs bind to SH groups, such as in cysteine, and directly interrupt the function of specific enzymes or break S–S bridges. These S-S bridges are necessary to maintain the integrity of folded proteins, and their breakage causes detrimental effects to the metabolism and physiology of the bacterial cell [66-68].

Rasheed et al. [69] demonstrated that palladium/tungsten oxide-supported graphene nanocomposites activate persulfate to generate ROS, including sulfate radicals, achieving efficient *E. coli* inactivation through advanced oxidation mechanisms. Similar ROS-mediated oxidative damage has been widely mentioned as a critical antibacterial pathway for metallic NPs. The oxidative stress-related antibacterial behavior has also been reported for ZnO nanostructures, where defect-rich ZnO NPs generate high levels of ROS and enhance antibacterial activity [70].

The size and shape of the nanoparticles have a great impact on the antibacterial activity. The smaller particles have a higher antibacterial activity [71]. The Pd nanoparticles can penetrate the cell membrane, causing structural and morphological changes and death [67, 72]. Fang et al. [25] reported that palladium nanocrystal facets presented enhanced membrane penetration against Gram-negative bacteria. However, some studies reported that larger NPs are more effective, indicating that size is not the only factor for their toxicity [73, 74]. Other factors include the formulation process, the environment, the bacterial defense mechanism, and the physical characteristics of the NP [68]. This study indicates that using AA shows better antibacterial properties than the chemical reducing agents of BH and HH, as it produces small Pd NPs onto AC in addition to being a green reducing agent (Fig. 13).

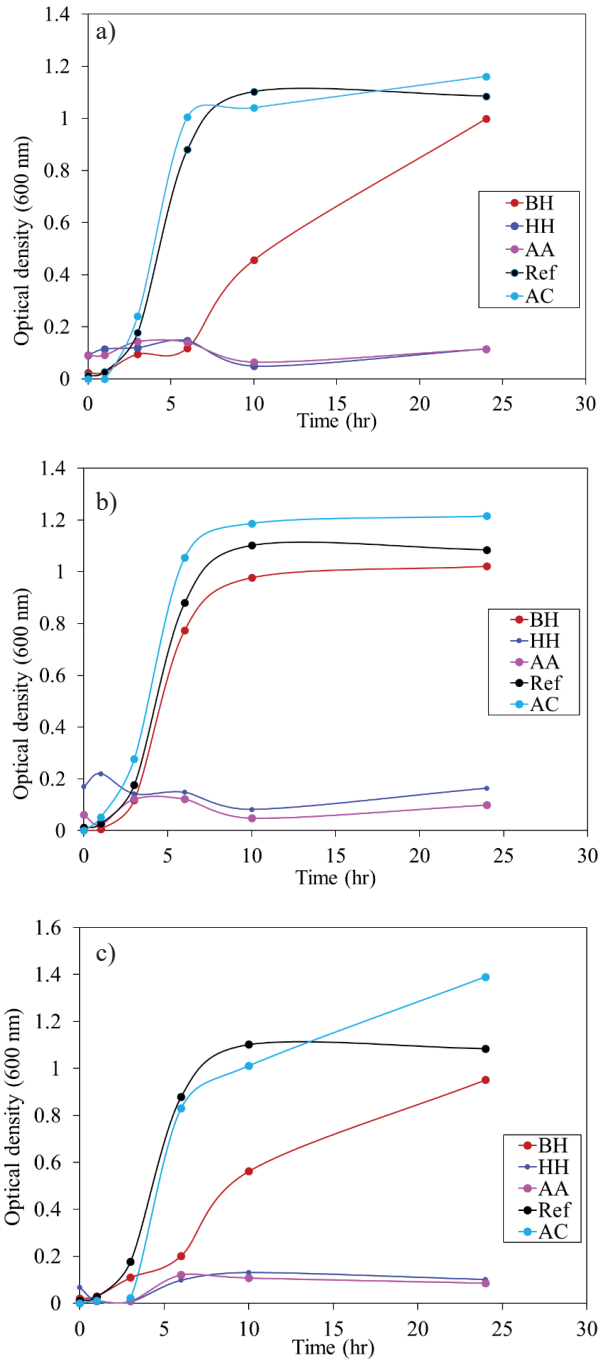

Fig. 13. Bacterial growth kinetics (optical density at 600 nm) for a) *E. coli*, b) *S. aureus,* and c) *B. cereus* using AC-Pd NPs reduced by BH, HH, and AA.

Conclusions

Activated carbon from black cumin seeds, in this study, was used as a support onto which Pd NPs were deposited using green (ascorbic acid) and chemical (borohydride and hydrazine hydrate) reducing agents. The particle size of Pd^0 varies between SEM and TEM. Pd NPs were evidently small when AA or HH were used, unlike Pd NPs produced by BH, which were large. As the reducing agent concentration increases, particle size also increases; however, the average crystallite size decreases. The antibacterial efficiency against *E. coli*, S. *aureus,* and *B. cereus* seems dependent on Pd particle size. Pd NPs produced by AA (2 mM) exhibited a smaller particle size and better antibacterial activity compared to those reduced by BH and HH. This demonstrates the importance of an appropriate reduction mechanism in controlling nanoparticles' characteristics to optimize their antibacterial performance.

Acknowledgments

The authors wish to thank the Deanship of Postgraduate Studies at Sultan Qaboos University for the support received. The authors also wish to thank the Research Council (TRC), Oman, for the Graduate Research Grant, GRG, with grant number (BFP/GRG/EBR/23/043), which supported the completion of this research.

AI Usage Disclosure Statement

Gemini 3.1 pro was utilized as a search engine in the introduction. The authors reviewed and are fully responsible for the final content.

Conflict of Interest

The authors declare no conflict of interest.

References

1. SRIVASTAV A.L., PATEL N., CHAUDHARY V.K. Disinfection by-products in drinking water: Occurrence, toxicity and abatement. Environmental Pollution, **267**, 115474, **2020**.
2. MISHRA A., PRADHAN D., HALDER J., BISWASROY P., RAI V.K., DUBEY D., KAR B., GHOSH G., RATH G. Metal nanoparticles against multi-drug-resistance bacteria. Journal of Inorganic Biochemistry, **237**, 111938, **2022**.
3. DIXIT A., KUMAR N., KUMAR S., TRIGUN V. Antimicrobial resistance: Progress in the decade since emergence of New Delhi Metallo-β-lactamase in India. Indian Journal of Community Medicine, **44** (1), 4, **2019**.
4. HU Z. T., CHEN Y., FEI Y. F., LOO S. L., CHEN G., HU M., SONG Y., ZHAO J., ZHANG Y., WANG J. An overview of nanomaterial-based novel disinfection technologies for harmful microorganisms: Mechanism, synthesis, devices and application. Science of The Total Environment, **837**, 155720, **2022**.
5. RAI M.K., DESHMUKH S.D., INGLE A.P., GADE A.K. Silver nanoparticles: the powerful nanoweapon against multidrug-resistant bacteria: activity of silver nanoparticles against MDR bacteria. Journal of Applied Microbiology, **112** (5), 841, **2012**.
6. OKKEH M., BLOISE N., RESTIVO E., DE VITA L., PALLAVICINI P., VISAI L. Gold nanoparticles: can they

be the next magic bullet for multidrug-resistant Bacteria? Nanomaterials, **11** (2), 312, **2021**.
7. ZOIDIS E., SEREMELIS I., KONTOPOULOS N., DANEZIS G. Selenium-dependent antioxidant enzymes: actions and properties of selenoproteins. Antioxidants, **7** (5), 66, **2018**.
8. MAHMOODI S., ELMI A., HALLAJ-NEZHADI S. Copper nanoparticles as antibacterial agents. Journal of Molecular Pharmaceutics and Organic Process Research, **6** (1), 1, **2018**.
9. MUBARAKALI D., KIM H., VENKATESH P.S., KIM J.W., LEE S.Y. A Systemic review on the synthesis, characterization, and applications of palladium nanoparticles in biomedicine. Applied Biochemistry and Biotechnology, **195** (6), 3699, **2023**.
10. CHEN A., OSTROM C. Palladium-Based Nanomaterials: Synthesis and Electrochemical Applications. Chemical Reviews, **115** (21), 11999, **2015**.
11. KUMAR A.P., PREM KUMAR B. KIRAN KUMAR A.B.V., THE HUY B., LEE Y.-I. Preparation of palladium nanoparticles on alumina surface by chemical co-precipitation method and catalytic applications. Applied Surface Science, **265**, 500, **2013**.
12. NEMAMCHA A., REHSPRINGER J.-L., KHATMI D.K. Synthesis of Palladium Nanoparticles by Sonochemical Reduction of Palladium(II) Nitrate in Aqueous Solution. Journal of Physical Chemistry B, **110** (1), 383, **2006**.
13. GUO R., ZHANG K., LIU Y., HE Y., WU C., JIN M. Hydrothermal synthesis of palladium nitrides as robust multifunctional electrocatalysts for fuel cells. Journal of Materials Chemistry A, **9** (10), 6196, **2021**.
14. SHRIVASTAV A., KHAPEKAR Y., SONI D., SANKATHALA S., DAS S. Green Synthesis of Palladium Nanoparticles Using Medicinally Important Plant Extracts. Transactions of the Indian Institute of Metals, **78** (4), 95, **2025**.
15. FERNÁNDEZ-ARIAS M., VILAS A.M., BOUTINGUIZA M., RODRÍGUEZ D., ARIAS-GONZÁLEZ F., POU-ÁLVAREZ P., RIVEIRO A., GIL J., POU J. Palladium nanoparticles synthesized by laser ablation in liquids for antimicrobial applications. Nanomaterials, **12** (15), 2621, **2022**.
16. AL-FAKEH M.S., OSMAN S.O.M., GASSOUMI M., RABHI M., OMER M. Characterization, antimicrobial and anticancer properties of palladium nanoparticles biosynthesized optimally using Saudi propolis. Nanomaterials, **11** (10), 2666, **2021**.
17. NARAYANAN R., EL-SAYED M.A. Catalysis with Transition Metal Nanoparticles in Colloidal Solution: Nanoparticle Shape Dependence and Stability. Journal of Physical Chemistry B, **109** (26), 12663, **2005**.
18. AL-SALEM L., SEOUDI R. Influence of ascorbic acid as modifier on the particle size and the optical properties of ZnO nanoparticles. Journal of Material Science: Material Electronics, **31**, 22642, **2020**.
19. RAZA M.A., KANWAL Z., RAUF A., SABRI A.N., RIAZ S., NASEEM S. Size- and Shape-Dependent Antibacterial Studies of Silver Nanoparticles Synthesized by Wet Chemical Routes. Nanomaterials, **6** (4), 74, **2016**.
20. BUŽKOVÁ A., HOCHVALDOVÁ L., VEČEŘOVÁ R., MALINA T., PETR M., KAŠLÍK J., KVÍTEK L., KOLÁŘ M., PANÁČEK A., PRUCEK R. Selenium nanoparticles: influence of reducing agents on particle stability and antibacterial activity at biogenic concentrations. Nanoscale, **17** (13), 8170, **2025**.
21. PALLIYARAYIL A., SELVARAJAN P., PRAKASH P.S., SATHISH C.I., DASIREDDY V.D., VINU A., KUMAR N.S., SIL S. An experimental and theoretical investigation on the oxidation of CO over Pd/C derived from the spent Pd catalyst. ChemCatChem, **13** (5), 1326, **2021**.
22. YASMIN S., KABI M.H., ROY N., JEON S. The effect of reducing agent for synthesizing palladium nanoparticle on carbon nanotube support and its superior catalytic activity towards methanol oxidation reaction. ECS Advances, **2** (2), 024504, **2023**.
23. RZELEWSKA-PIEKUT M., WOLAŃCZYK Z., NOWICKI M., REGEL-ROSOCKA M. Precipitation of Pt, Pd, Rh, and Ru Nanoparticles with Non-Precious Metals from Model and Real Multicomponent Solutions. Molecules, **28** (13), 5188, **2023**.
24. MENDES A.R., GRANADEIRO C.M., LEITE A., PEREIRA E., TEIXEIRA P., POÇAS F. Optimizing antimicrobial efficacy: Investigating the impact of zinc oxide nanoparticle shape and size. Nanomaterials, **14** (7), 638, **2024**.
25. FANG G., LI W., SHEN X., PEREZ-AGUILAR J.M., CHONG Y., GAO X., CHAI Z., CHEN C., GE C., ZHOU R. Differential Pd-nanocrystal facets demonstrate distinct antibacterial activity against Gram-positive and Gram-negative bacteria. Nature Communications, **9** (1), 129, **2018**.
26. ELTUGRAL N., SIMSIR H., KARAGOZ S. Preparation of nano-silver-supported activated carbon using different ligands. Research on Chemical Intermediates, **42** (3), 1663, **2016**.
27. YU B., WANG X., QIAN X., XING W., YANG H., MA L., LIN Y., JIANG S., SONG L., HU Y., LO S. Functionalized graphene oxide/phosphoramide oligomer hybrids flame retardant prepared via in situ polymerization for improving the fire safety of polypropylene. RSC Advances, **4** (60), 31782, **2014**.
28. CZERWIŃSKA-GŁÓWKA D., KRUKIEWICZ K. Guidelines for a morphometric analysis of prokaryotic and eukaryotic cells by scanning electron microscopy. Cells, **10** (12), 3304, **2021**.
29. GRAHAM L., ORENSTEIN J.M. Processing tissue and cells for transmission electron microscopy in diagnostic pathology and research. Nature Protocols, **2** (10), 2439, **2007**.
30. YANG X. A Study on Antimicrobial Effects of Nanosilver for Drinking Water Disinfection, (Springer Theses). Springer**2017**.
31. DÍEZ-PASCUAL A.M. Antibacterial activity of nanomaterials. Nanomaterials, **8** (6), 359, **2018**.
32. PARVEEN N., GOEL S. Trihalomethane cancer risk assessment for private and shared residences: addressing the differences in inhalation exposure. Toxics, **11** (4), 295, **2023**.
33. MALATO S., FERNÁNDEZ-IBÁÑEZ P., MALDONADO M.I., BLANCO J., GERNJAK W. Decontamination and disinfection of water by solar photocatalysis: recent overview and trends. Catal. Today, **147** (1), 1, **2009**.
34. AL-ABRI M., AL-GHAFRI B., BORA T., DOBRETSOV S., DUTTA J., CASTELLETTO S., ROSA L. BORETTI A. Chlorination disadvantages and alternative routes for biofouling control in reverse osmosis desalination. NPJ Clean Water, **2** (1), 2, **2019**.
35. DIZDAROGLU M. Substrate specificities and excision kinetics of DNA glycosylases involved in base-excision repair of oxidative DNA damage. Mutation Research, **531** (1-2), 109, **2003**.

36. RAI M., YADAV A., GADE A. Silver nanoparticles as a new generation of antimicrobials. Biotechnology Advances, **27** (1), 76, **2009**.
37. LEMIRE J.A., HARRISON J.J., TURNER R.J. Antimicrobial activity of metals: mechanisms, molecular targets and applications. Nature Reviews Microbiology, **11** (6), 371, **2013**.
38. FRANCO D., CALABRESE G., GUGLIELMINO S.P.P., CONOCI S. Metal-based nanoparticles: antibacterial mechanisms and biomedical application. Microorganisms, **10** (9), 1778, **2022**.
39. BAPTISTA P.V., MCCUSKER M.P., CARVALHO A., FERREIRA D.A., MOHAN N.M., MARTINS M., FERNANDES A.R. Nano-strategies to fight multidrug resistant bacteria-"A Battle of the Titans". Frontiers in Microbiology, **9**, 1441, **2018**.
40. RODRIGUES T.S., ZHAO M., YANG T.H., GILROY K.D., DA SILVA A.G., CAMARGO P.H., XIA Y. Synthesis of colloidal metal nanocrystals: A comprehensive review on the reductants. Chemistry - A European Journal, **24** (64), 16944, **2018**.
41. QUINSON J., JENSEN K.M.Ø. From platinum atoms in molecules to colloidal nanoparticles: A review on reduction, nucleation and growth mechanisms. Advances in Colloid and Interface Science, **286**, 102300, **2020**.
42. LU J., DREISINGER D.B., COOPER W.C. Cobalt precipitation by reduction with sodium borohydride. Hydrometallurgy, **45** (3), 305, **1997**.
43. VANYSEK P. Electrochemical series, CRC handbook of Chemistry and Physics **8**, 8, **2000**.
44. AL AZWANI M.A., AL BUSAFI S., EL-SHAFEY E.S.I. Preparation and characterization of graphene oxide-based cation, chelating, and anion exchangers for salt removal. Heliyon, **11** (3), e42070, **2025**.
45. JOHNSON M.R., RICKBORN B. Sodium borohydride reduction of conjugated aldehydes and ketones. Journal of Organic Chemistry, **35** (4), 1041, **1970**.
46. NEUMAN R.C. Jr Oxidation and reduction, Organic Chemistry, **17**, 0-38, **2008**.
47. PALOMBA M., CAROTENUTO G., LONGO A. A brief review: the use of L-ascorbic acid as a green reducing agent of graphene oxide. Materials, **15** (18), 6456, **2022**.
48. MOLAEI R., FARHADI K., FOROUGH M., HAJIZADEH S. Green biological fabrication and characterization of highly monodisperse palladium nanoparticles using Pistacia atlantica fruit broth. Journal of Nanostructures, **8** (1), 47, **2018**.
49. LANGFORD J.I., WILSON A.J.C. Scherrer after sixty years: a survey and some new results in the determination of crystallite size. Journal of Applied Crystallography, **11** (2), 102, **1978**.
50. AJITHA B., REDDY P.S. Reducing Agent Concentration dependence on Size variation of Silver Nanoparticles growth. International Journal of ChemTech Research, **6** (3), 2123, **2014**.
51. THANH N.T., MACLEAN N., MAHIDDINE S. Mechanisms of nucleation and growth of nanoparticles in solution. Chemical Reviews, **114** (15), 7610, **2014**.
52. DUNIN-BORKOWSKI R.E., FEUERBACHER M., HEGGEN M. F1 Advanced Transmission Electron Microscopy Techniques and Applications. Lecture Notes of the 43rd IFF Spring School "Scattering Methods for Condensed Matter Research: Towards Novel Applications at Future Sources", Forschungszentrum Jülich, **2012**.
53. KORCHINSKI D.J., DUERETH J., MCNEIL R., AU M., SCHMID V. A Brief Introduction to Scanning Electron Microscopy, **2019**.
54. NOLLET H., ROELS M., LUTGEN P., VAN DER MEEREN P., VERSTRAETE W. Removal of PCBs from wastewater using fly ash. Chemosphere, **53** (6), 655, **2003**.
55. BERGERET G., GALLEZOT P. Particle size and dispersion measurements. Handbook of Heterogeneous Catalysis, **2**, 738, **2008**.
56. EL-SHAFEY E.S.I., AL-LAWATI H.A., AL-SAIDI W.S. Adsorption of lisinopril and chlorpheniramine from aqueous solution on dehydrated and activated carbons. Carbon Letters, **19**, 12, **2016**.
57. KIM H.S., SEO Y.S., KIM K., HAN J.W., PARK Y., CHO, S. Concentration effect of reducing agents on green synthesis of gold nanoparticles: size, morphology, and growth mechanism. Nanoscale Research Letters, **11**, 230, **2016**.
58. AGNIHOTRI S., MUKHERJI S., MUKHERHERJI S. Size-controlled silver nanoparticles synthesized over the range 5-100 nm using the same protocol and their antibacterial efficacy. RSC Advances, **4** (8), 3974, **2014**.
59. DEVI T.B., MOHANTA D., AHMARUZZAMAN M. Biomass derived activated carbon loaded silver nanoparticles: An effective nanocomposite for enhanced solar photocatalysis and antimicrobial activities. Journal of Industrial and Engineering Chemistry, **76**, 160, **2019**.
60. JEONG H.Y., LEE J.H., HAYES K.F. Characterization of synthetic nanocrystalline mackinawite: crystal structure, particle size, and specific surface area. Geochimica et Cosmochimica Acta, **72** (2), 493, **2008**.
61. SHANTHI P.M., HANUMANTHA P.J., RAMALINGA K., GATTU B., DATTA M.K., KUMTA P.N. Sulfonic acid based complex framework materials (CFM): nanostructured polysulfide immobilization systems for rechargeable lithium-sulfur battery. Journal of The Electrochemical Society, **166** (10), A1827, **2019**.
62. TAHIR K., NAZIR S., LI B., AHMAD A., NASIR T., KHAN A.U., SHAH S.A.A., KHAN Z.U.H., YASIN G., HAMEED M.U. Sapium sebiferum leaf extract mediated synthesis of palladium nanoparticles and in vitro investigation of their bacterial and photocatalytic activities. Journal of Photochemistry and Photobiology B, **164**, 164, **2016**.
63. CHEN Y., CHEN Z., YANG D., ZHU L., LIANG Z., PANG Y., ZHOU L. Novel microbial palladium nanoparticles with a high photothermal effect for antibacterial applications. ACS Omega, **8** (1), 1534, **2023**.
64. AMEEN F., KARIMI-MALEH H., DARABI R., AKIN M., AYATI A., AYYILDIZ S., BEKMEZCI M., BAYAT R., SEN F. Synthesis and characterization of activated carbon supported bimetallic Pd based nanoparticles and their sensor and antibacterial investigation. Environmental Research, **221**, 115287, **2023**.
65. HAZARIKA M., BORAH D., BORA P., SILVA A.R., DAS P. Biogenic synthesis of palladium nanoparticles and their applications as catalyst and antimicrobial agent. PLoS One, **12**, e0184936, **2017**.
66. MA J.X., CHEN X.L., HUANG M.X. Understanding the antibacterial mechanism of metal surfaces. Acta Biomater, **192**, 501, **2025**.
67. SALMAN S.H., KHASHAN K.S., HADI A.A. Green synthesis and characterization of palladium nanoparticles by pulsed laser ablation and their antibacterial activity. Metals, **13** (2), 273, **2023**.

68. SLAVIN Y.N., ASNIS J., HÄFELI U.O., BACH H. Metal nanoparticles: understanding the mechanisms behind antibacterial activity. Journal of Nanobiotechnology, **15** (1), 65, **2017**.
69. RASHEED F.A., IBRAHIM H.M., VIASI F., ALI S.M. Persulfate activation using a novel palladium/tungsten (III) oxide-supported graphene nanocomposite for *Escherichia coli* inactivation: Efficiency, mechanisms, and stability. Desalination and Water Treatment, **317**, 100285, **2024**.
70. SATHE P., LAXMAN K., MYINT M.T.Z., DOBRETSOV S., RICHTER J., DUTTA J. Bioinspired nanocoatings for biofouling prevention by photocatalytic redox reactions. Scientific Reports, **7** (1), 3624, **2017**.
71. DA SILVA B.L., CAETANO B.L., CHIARI-ANDRÉO B.G., PIETRO R.C.L.R., CHIAVACCI L.A. Increased antibacterial activity of ZnO nanoparticles: Influence of size and surface modification. Colloids and Surfaces B: Biointerfaces, **177**, 440, **2019**.
72. WEINSTEIN M.P., LEWIS J.S. The clinical and laboratory standards institute subcommittee on antimicrobial susceptibility testing: background, organization, functions, and processes. Journal of Clinical Microbiology, **58** (3), e01864-19, **2020**.
73. EL BADAWY A.M., SILVA R.G., MORRIS B., SCHECKEL K.G., SUIDAN M.T., TOLAYMAT T.M. Surface charge-dependent toxicity of silver nanoparticles. Environmental Science & Technology, **45** (1), 283, **2011**.
74. SOHM B., IMMEL F., BAUDA P., PAGNOUT C. Insight into the primary mode of action of TiO_2 nanoparticles on *Escherichia coli* in the dark. Proteomics, **15** (1), 98, **2015**.

Sulplimentary Material

Lin to Sulplimentary Material https://www.pjoes.com/SuppFile/224840/1/